Analyst

PAPER

View Article Online
View Journal

Cite this: DOI: 10.1039/c8an00234g

In vitro antibacterial activity of oxide and non-oxide bioceramics for arthroplastic devices: II. Fourier transform infrared spectroscopy

Francesco Boschetto,[a,b] Nami Toyama,[a] Satoshi Horiguchi,[c] Ryan M. Bock,[d] Bryan J. McEntire,[d] Tetsuya Adachi,[c] Elia Marin,[a,c] Wenliang Zhu,[a] Osam Mazda,[b] B. Sonny Bal[d,e] and Giuseppe Pezzotti *[a,b,f,g,h]

Received 6th February 2018,
Accepted 3rd April 2018

DOI: 10.1039/c8an00234g

rsc.li/analyst

The metabolic response of Gram-positive *Staphylococcus epidermidis* (*S. epidermidis*) bacteria to bioceramic substrates was probed by means of Fourier transform infrared spectroscopy (FTIR). Oxide zirconia-toughened alumina (ZTA) and non-oxide silicon nitride (Si_3N_4) substrates were tested. Bacteria exposed to silica glass substrates were used as a control. *S. epidermidis*, a major cause of periprosthetic infections, was screened to obtain a precise time-lapse knowledge of its molecular composition and to mechanistically understand its interaction with different substrates. At the molecular level, the structure of proteins, lipids, nucleic acid, and aromatic amino acids evolved with time in response to different substrates. In combination with statistical validation and local pH measurements, a chemical lysis mechanism was spectroscopically observed *in situ* on the Si_3N_4 substrates. Utilization of FTIR in this study avoided fluorescence noise which occurred while probing the ZTA samples with Raman spectroscopy in a companion paper. The substrate-driven dynamics of polysaccharide and peptide variations in the bacterial cell wall, peculiar to Si_3N_4 bioceramics, are elucidated.

1. Introduction

Several research groups have recently shown the potential of vibrational spectroscopy in accessing precise compositional and structural information from living bacterial cells.[1–8] FTIR absorption and Raman spectroscopies have provided rich spectral "fingerprints" of cell metabolism. Coupled with traditional microbiological methods, they have been helpful in characterizing the antibacterial potential of specific drugs and biomaterial substrates.[9,10] The ability to probe vibrational changes with high efficiency in dipole moment (*e.g.*, C═O stretching vibrations) makes FTIR absorption particularly suitable for detecting chemical variations in both the amide bonds of peptides within proteins and in acids or esters within lipids.[11] In a complementary way, the Raman emission excited in the visible wavelength region is sensitive to chemical moieties exhibiting high polarizability (*e.g.*, ring and C–C vibrations).[12] The Raman emission exhibits low scattering efficiency but, unlike FTIR, it can be easily collected with high spatial resolution. Accordingly, Raman spectra have been used to record local changes associated with growth and lysis of bacteria[12–14] and to assess early infections.[15]

The pathogenic mechanisms by which *staphylococci* induce persistent periprosthetic infections as well as their capacity to resist antibiotics have been the object of several studies.[16–18] The virulence of *S. epidermidis* in periprosthetic infections is a serious issue in orthopedics[19] and a consequence of its enhanced ability to form a biofilm on the surface of synthetic biomaterials.[20–22] Biofilms consist of multilayered cell clusters rooted in a slime matrix made up of polysaccharides (glycosaminoglycans) and bacterial membrane moieties.[21] Bacterial adhesion, aggregation, successive proliferation, and slime production represent a cascade of events behind virulent and persistent *S. epidermidis* infections.[22] Characterization of the these metabolic steps may pave the way to understanding infection chemistry, the bacteria's ability to differ-

[a]*Ceramic Physics Laboratory, Kyoto Institute of Technology, Kyoto, Japan. E-mail: pezzotti@kit.ac.jp*
[b]*Department of Immunology, Kyoto Prefectural University of Medicine, Kamigyo-ku, Kyoto 602-8566, Japan*
[c]*Department of Dental Medicine, Graduate School of Medical Science, Kyoto Prefectural University of Medicine, Kamigyo-ku, Kyoto 602-8566, Japan*
[d]*Amedica Corporation, Salt Lake City, UT, USA*
[e]*Department of Orthopaedic Surgery, University of Missouri, Columbia, MO, USA*
[f]*Department of Orthopedic Surgery, Tokyo Medical University, Tokyo, Japan*
[g]*The Center for Advanced Medical Engineering and Informatics, Osaka University, Osaka, Japan*
[h]*The Center for Advanced Insect Research Promotion (CAIRP), Kyoto Institute of Technology, Kyoto, Japan*

entiate slime characteristics in drug-resistant biofilms, and the desirable design features of new biomaterials that inherently possess antibacterial mechanisms.

In this paper, the evolution of the FTIR spectrum of *S. epidermidis* bacteria exposed to oxide and non-oxide bioceramics is examined in an attempt to understand how bacterial structure and molecular composition are altered in relation to the chemistry of different bioceramic substrates. The consequence of these chemical reactions at the bacteria/substrate interface could ultimately lead to chemical lysis. The metabolism of *S. epidermidis* bacteria was interpreted through their FTIR spectra recorded in time-lapse experiments in comparison with Raman data previously collected from the same samples and reported in a companion paper.[23] Environmental data around the substrates were collected using pH microscopy as a compliment to the vibrational spectroscopy. Unlike Raman spectroscopy, the FTIR spectra collected on the ZTA substrates were found to be unaffected by a fluorescence noise arising from a fraction of Cr-oxide dopant intentionally added during manufacturing. This circumstance enabled a direct comparison between spectra collected on oxide and non-oxide bioceramics under the same testing conditions.

2. Experimental procedures

Both ZTA and Si_3N_4 substrates were obtained from commercially available sources. Si_3N_4 samples (Ø 12.7 × 1.0 mm, Amedica Corp., Salt Lake City, UT) were pressed and sintered from a high-purity powder (Ube SN E-10, Ube City, Japan). Yttrium oxide (Y_2O_3, Grade C, H. C. Starck, Munich, Germany) and aluminum oxide (Al_2O_3, SA8-DBM, Baikowski/Malakoff, Charlotte, NC) were used as sintering aids. The full details for the fabrication of the Si_3N_4 sintered substrates have been reported in ref. 24. Briefly, the $Si_3N_4/Y_2O_3/Al_2O_3$ powder mixture was formed at room temperature into a green body with plate geometry. The green body was then sintered in a nitrogen atmosphere at a temperature in excess of 1700 °C in order to close the surface porosity, and further densified by hot isostatic pressing at a temperature exceeding 1650 °C under a N_2 gas pressures >200 MPa. The resulting Si_3N_4 exhibited a two-phase microstructure mainly consisting of anisotropic β-Si_3N_4 grains separated by thin (<2 nm) grain boundaries of amorphous or crystalline yttrium aluminum oxynitride or Si(Y)AlON, respectively. ZTA disks of the same geometry were obtained by machining and finely polishing BIOLOX®*delta* femoral head components (CeramTec, GmbH, Plochingen, Germany). This ZTA contained 80 vol% Al_2O_3, 17 vol% zirconia (ZrO_2), and 3 vol% chromium oxide (Cr_2O_3), largely dissolved in solid solution with Al_2O_3. A minor amount of strontium oxide (SrO) was also added which reacted to form strontium-aluminate ($SrAl_2O_4$) platelets during firing.[25] All bioceramic substrates were polished to mirror finishes before testing.

Local pH mapping experiments were conducted using a pH microscope (SCHEM-110; Horiba, Kyoto, Japan) capable of measuring pH values at the surface of solids with high spatial resolution (100 μm). In order to perform pH microscopy experiments, ceramic substrates were fully embedded into an acidic gel consisting of artificial saliva, KCl, and agar. The pH-imaging sensor consisted of a flat semiconductor plate with a total sensing area of 2.5 × 2.5 cm^2. The pH sensitivity of the sensor was 0.1 pH. The instrument utilized a light addressable potentiometric sensor, capable of detecting protons within the electrolyte medium. A light beam was directed from the back of the sensor with a bias voltage applied between the electrolyte and the back. The AC photocurrent induced by the modulated illumination was measured. This parameter depended on the amount of protons at the sensor surface, from which the pH value was determined.[26] Software conversion (Image Pro Plus, Media Cybernetics, Rockville, MD, USA) of local pH values into a color scale created a pH image recordable as a function of time. After embedding samples into the acidic gel, pH maps were obtained at various time intervals up to 45 min.

S. epidermidis (14990®ATCC™) cells were cultured in heart infusion (HI) broth (Nissui, Tokyo, Japan) at 37 °C for 18 hours and titrated by colony forming assay using brain heart infusion (BHI) agar (Nissui). After dilution with a phosphate-buffered saline (PBS) at physiological pH and ionic strength, each 100 μl of the bacterial suspension at a density of 1 × 10^8 CFU ml^{-1} was spread onto a BHI agar plate. The ceramic substrate samples were UV sterilized, and pressed into the bacteria on BHI agar for inoculation. They were then incubated at 37 °C under aerobic conditions for 12, 24, and 48 hours.

Time-lapse FTIR spectra were collected after exposing the cultured *S. epidermidis* bacterial cells to different bioceramic and glass control substrates. FTIR spectra were acquired using a high sensitivity microscope (Spectrum100FT-IR/Spotlight400; PerkinElmer Inc., Waltham, MA, USA). The spectral resolution of this equipment was 0.4 cm^{-1}. Substrate samples exposed to bacteria in BHI agar at 37 °C were removed after 12, 24, and 48 hours. They retained the bacterial cells on their surface and were introduced into the FTIR equipment without drying or any further manipulation. Average FTIR spectra were computed for each substrate using 5 independent measurements performed on $n = 4$ samples for each type of substrate. Spectral acquisition and pre-processing of raw data, which included baseline subtraction, smoothing, normalization and fitting of the raw spectra, were carried out using commercially available software (Origin 8.5, OriginLab Co., Northampton, MA, USA). The unpaired Student's *t*-test was utilized for statistical analyses; p values <0.05 were considered statistically significant and labeled with an asterisk.

3. Results

3.1. pH buffering effect in Si_3N_4 bioceramics

In Fig. 1(a), time-lapse maps are shown which represent the pH evolution at the interface of the Si_3N_4 substrate and acidic

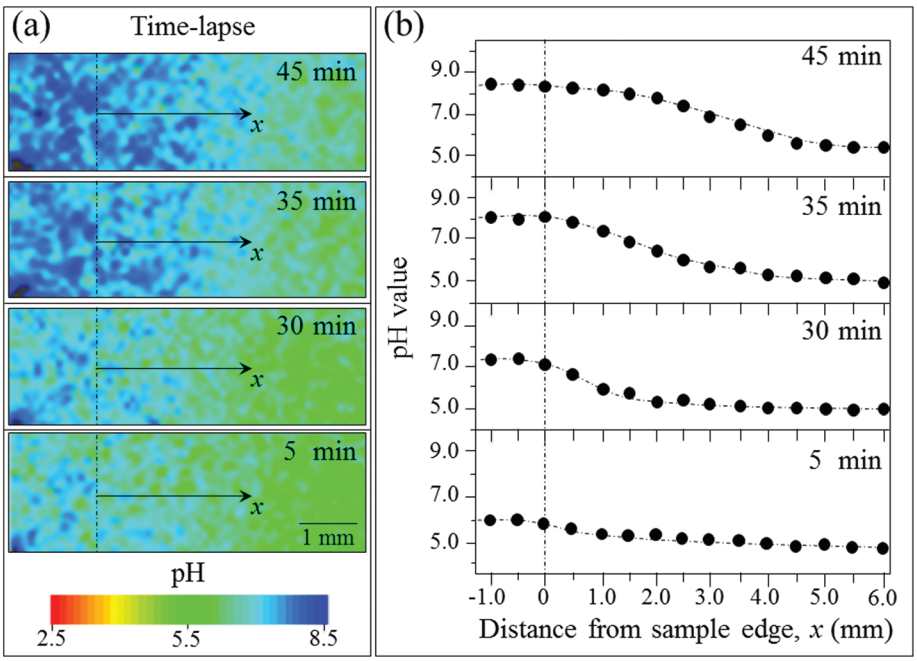

Fig. 1 (a) Time-lapse (*cf.* time in the inset) maps of pH near the interface between a Si_3N_4 substrate and an acidic gel (pH ~ 4.5); (b) average pH profiles along the *x*-axis extracted from the maps in (a) as a function of time.

gel (initial pH~4.5). There was a gradual conversion of the acidic gel surrounding the Si_3N_4 sample from acidic to alkaline (pH~8.5) in a relatively short time frame (~45 min). This buffering action is quantitatively shown in Fig. 1(b) by averaging the pH profiles computed from the maps taken at each time point. These same experiments were repeated with a ZTA substrate. Plots as a function of time of the average pH values recorded on the top of both Si_3N_4 and ZTA substrates are given in Fig. 2. The pH-buffering effect was only observed for the non-oxide substrate.

3.2. Labeling the infrared spectrum of *S. epidermidis*

There is an FTIR absorbance activity zone which is sensitive to the structural variations of *S. epidermidis*'s nucleic acids and polysaccharides in the frequency range between 1000–1460 cm^{-1} (referred to as Zone I).[2] In this region, there are 27 sub-bands which relate to a number of specific bonds: (i) Amide III bands with their maxima located between 1268 and 1314 cm^{-1}; (ii) C–OH stretching and in-plane bending modes (1165 and 1417 cm^{-1}, respectively); (iii) C–O–C glycosidic bonds between 1000 and 1200 cm^{-1}; (iv) C–O bonds (cumulative of different species including carbohydrates and phospholipids) at 1064, 1145, and 1186 cm^{-1}; and, (v) P═O symmetric (1078 and 1212 cm^{-1}), and antisymmetric (1225 and 1239 cm^{-1}) stretching of PO_2 in membrane and nucleic acids.[27] All the individual bands expected to appear in this zone are listed in Table 1 together with their physical origin and literature ref. 2, 4 and 27–37. However, there was broad spectral activity also from the silica glass control samples that overlapped this region. Accordingly, only spectra collected from the ceramic substrates were used for comparing the time-lapse spectral evolution of the bacteria. Nevertheless, the spectral zone 1460–1800 cm^{-1} (Zone II) is shown in Fig. 3 for the control sample after 12, 24, and 48 h of exposure to the silica glass substrates. Table 2 lists the adopted band labels in this zone together with their frequencies, physical origin, and literature ref. 4, 9, 32, 33, 36 and 38–41. Besides bands related to Amide I (1621–1698 cm^{-1}) and Amide II (1520–1570 cm^{-1}) vibrations, the broad absorbance activity at around 1600 cm^{-1} may also be affected by deprotonated carboxyl groups (COO^-) of bacterial peptides (discussed later). Moreover, the absorption band at 1637 cm^{-1} of the Amide I vibrations originated mainly from carbonyl groups (C═O) stretching, while the triplet localized at 1717, 1735, and 1742 cm^{-1} resulted from stretching of carbonic acid in lipids and fatty acids, ester

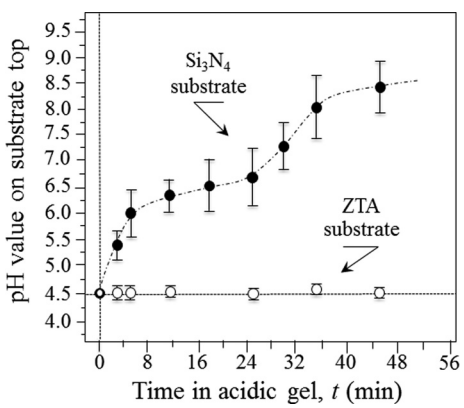

Fig. 2 Plots as a function of time of the average pH values recorded on top of Si_3N_4 and ZTA substrates.

Table 1 FTIR absorbances in the spectral Zone I in the frequency interval 1000–1460 cm^{-1}; band labels, physical origin and reference literature are shown for each absorbance peak frequency

Band	Assignment	Frequency (cm^{-1})	Ref.
1	C–O and C–C stretching of pyranose ring in polysaccharides	1030	24
2	C–C, C–OH, C–H, ring and side modes oligosaccharides	1044	25
3	C–O or P–O–C stretching phospholipids, $H_2PO_4^-$ antisymmetric stretching	1064	24, 26 and 27
4=	HPO_4^{2-} antisymmetric stretching	1072	26 and 27
4	P═O symmetric stretching of PO_2^- in DNA, RNA, and phospholipids	1078	28
5	C–O–C symmetric stretching in polysaccharides	1086	28
6	C–O carbohydrates, P═O stretching (symmetric) of PO_2^-	1093	28
7	C–O and C–C stretching in polysaccharide rings	1107	28 and 29
8	C–C stretching skeletal *trans* conformation in DNA/RNA	1120	29
9	PO_2^- (phospholipids) and C–O (carbohydrates) stretching	1145	30
10	C–O–P, C–C, C–O–H in DNA and RNA backbone	1165	29
11	C–O stretching in carbohydrates	1186	28
12	P═O bond symmetric stretching in phosphate	1212	31
13	P═O antisymmetric stretching of PO_2^- in phosphodiester	1225	4
14	P═O antisymmetric stretching in PO_2^-, protonated phosphonates	1240	26–28
15	C–O–C Amide III in proteins, C–OH in carboxylic acid	1268	28 and 32
16	Amide III	1286	28
17	Amide III	1296	29
18	Amide III	1314	28
19	Amide III	1338	29
20	Symmetric stretching of carboxyl groups in amino acid side chains or free fatty acids	1362	33
21	C–H deformation	1374	33
22	CH_3 asymmetric bending in peptidoglycans	1385	4
23	Deprotonated carboxyl groups (COO^-)	1396	4
24	O–C–O symmetric stretching of deprotonated COO^- in amino acid side chains and free fatty acids	1417	28 and 34
25	C–O–H in plane bending	1435	29
26	CH_2 symmetric bending in polysaccharides	1455	28

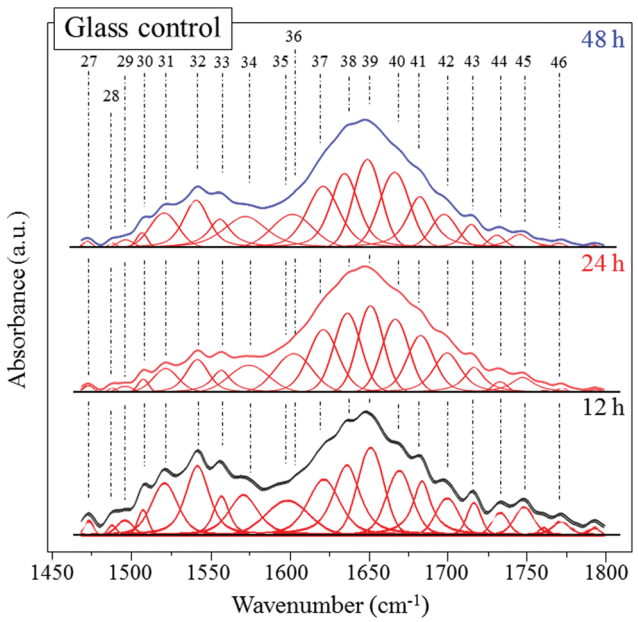

Fig. 3 The FTIR spectral Zone II in the frequency interval 1460–1800 cm^{-1} as observed on the *S. epidermidis* sample after 12, 24, and 48 h exposures to a silica glass control substrate. The labeling of the sub-bands corresponds to that shown in Table 2.

groups, and C═O in saturated esters, respectively. Finally the band at 1771 cm^{-1} was related to COOH protonated groups. Probing the time-lapse variations of the FTIR spectrum (*cf.* Fig. 3) on the control sample did not reveal any significant

Table 2 FTIR absorbances in the spectral Zone II in the frequency interval 1460–1800 cm^{-1}; the band labels, their physical origin and reference literature are shown for each absorbance peak frequency

Band	Assignment	Frequency (cm^{-1})	Ref.
27	CH, CH_2 in teichoic acids, peptido glycan and phospholipids	1473	28
28	CH, CH_2 in lipids and proteins	1482	28
29	C–C stretching in aromatic ring	1495	35
30	Carboxylic group in peptides	1505	33
31	Amide II	1520	28
31*	COO^- antisymmetric stretching of deprotonated carboxyl groups	1533	4 and 36
32	Amide II	1545	37
33	Amide II	1557	37
34	Amide II	1570	33
35	C–C stretching skeletal *trans* conformation in DNA/RNA COO^- antisymmetric stretching	1590	4 and 34
36	PO_2^- (phospholipids) and C–O (carbohydrates) stretching	1605	37
37	Amide I (β-sheet)	1621	38
38	Amide I (C═O stretching in carbonyl groups)	1637	28 and 29
39	Amide I (α-helix)	1652	28
40	Amide I (antiparallel sheets and β-turns)	1672	28
41	Amide I (antiparallel sheets and β-turns)	1683	28
42	Amide I (antiparallel sheets and β-turns)	1698	28
43	>C═O stretching of carbonic acid groups in lipids and fatty acids	1717	28
44	>C═O stretching of ester groups	1735	28
45	C═O stretching in saturate esters	1742	28
46	COOH protonated	1771	39

variation in the spectrum morphology in zone between 1600 and 1800 cm^{-1} (Bands labeled 35–46) at any of the exposure times. However, at lower frequencies, an initial reduction in relative intensity for the Amide II Bands 31 and 32 at 24 h was followed by an enhancement after 48 h. The conspicuously unchanged spectral morphology and the observed trend of Amide II bands are spectroscopic fingerprints demonstrating the healthy state of proliferating bacteria on the glass controls.[42]

3.3. Time-lapse FTIR spectra in different bioceramic substrates

Fig. 4 and 5 show the low-frequency (normalized) spectra of Zone I collected on *S. epidermidis* exposed to ZTA and Si_3N_4 substrates, respectively (*cf.* Table 1 for band labeling and physical origins). Time-lapse spectra are displayed in both figures with exposure times shown in the insets of the respective figures. For comparison, the normalized spectrum of unexposed *S. epidermidis* (taken as the "time-zero spectrum") is plotted in both figures in the frequency interval 1000–1230 cm^{-1}. In the case of the ZTA substrates (Fig. 4), the spectra in Zone I was rich in features and was normalized to Band 2 (at 1044 cm^{-1}; C–C, C–OH, and C–H ring and side group vibrational modes in oligosaccharides[29]). The main features are as follows:

(i) The change in the relative intensity of Band 6 at 1093 cm^{-1} (*i.e.*, more than a twofold increase) suggests a significant upsurge in both carbohydrates (C–O stretching) and PO_2^- moieties (P═O symmetric stretching). This was accompanied by a similar trend for Band 1 at ~1030 cm^{-1} related to polysaccharides. Note that, in the spectrum of unexposed bacteria normalized to Band 1 (*cf.* dotted line in Fig. 4 overlapped to the 48 h spectrum), Band 6 possessed a relatively lower intensity as compared to the spectra from exposed bacteria. This difference between spectra of substrate-exposed and unexposed bacteria could be explained as a reaction of the bacteria to the presence of the substrate. We hypothesize that the increased intensity contribution to Band 6 in substrate-exposed bacteria arose from thickening of the peptidoglycan layer on the external side of the bacterial membrane (*i.e.*, involving a larger fraction of carbohydrate C–O bonds and, accordingly, a stronger stretching emission).

(ii) Bacteria proliferation of during the time-lapse experiments was also observed *via* a dramatic increase in the relative intensity of Bands 10–13 within the absorbance interval 1165–1225 cm^{-1}. These bands include the DNA/RNA backbone, carbohydrate, and phosphate vibrations of *S. epidermidis* (*cf.* Table 1). Note that the overall increase in Raman intensity noted in this spectral region tends to approach the level for unexposed bacteria. There are, however, morphological differences between spectra of exposed and unexposed bacteria. In the case of exposed bacteria, Bands 12 and 13 are significantly less pronounced than Bands 10 and 11. The latter two bands (especially Band 11) are mainly contributed by C–O stretching in carbohydrates, while the former ones are from phosphate bonds in lipids and DNA. Accordingly, the observation of a stronger emission from carbohydrates supports the hypothesis of thickening of the

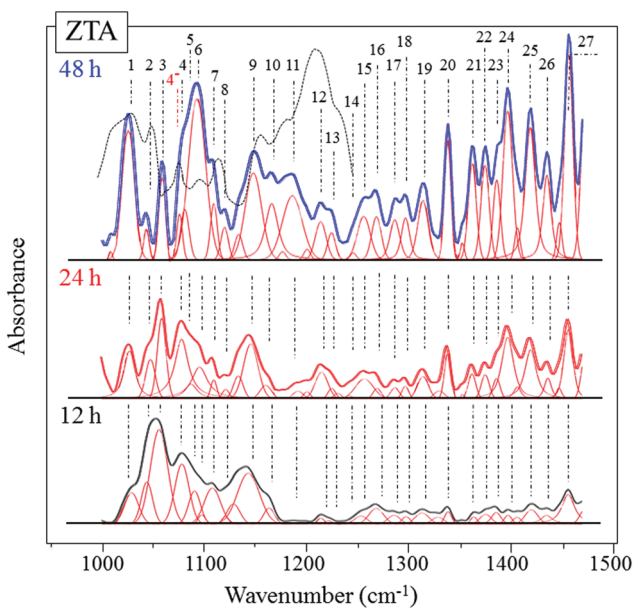

Fig. 4 The FTIR spectral Zone I after normalization as collected on the *S. epidermidis* sample exposed to ZTA substrates for increasing times (*cf.* labels in the inset). For comparison, the spectrum at time ~0 is shown as a dotted line overlapped to the spectrum collected at 48 h in the region 1000–1230 cm^{-1}. The labeling of the sub-bands corresponds to that shown in Table 1.

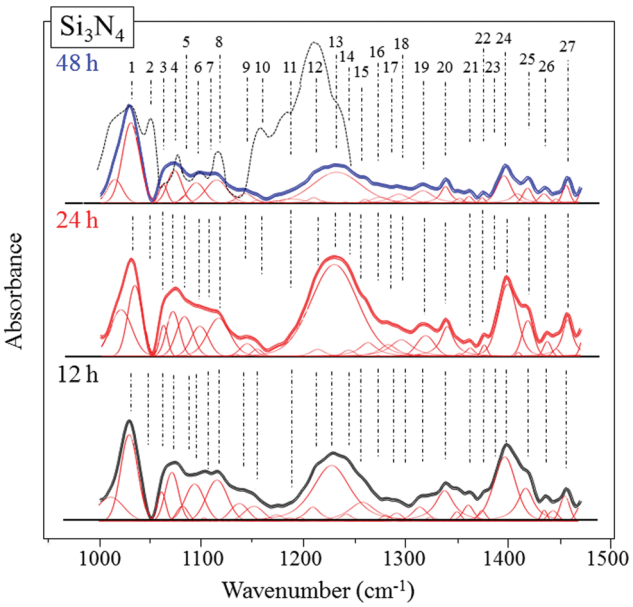

Fig. 5 The FTIR spectral Zone I after normalization on the *S. epidermidis* sample exposed to Si_3N_4 substrates for increasing times (*cf.* labels in the inset). For comparison, the spectrum at time ~0 is shown as a dotted line overlapped to the spectrum collected at 48 h in the region 1000–1230 cm^{-1}. The labeling of the sub-bands corresponds to that shown in Table 1.

outer peptidoglycan layer of the membrane when bacteria become exposed to the substrate (*cf.* above item (i)).

(iii) A significant increase in the Amide III Bands 16–19 within the frequency interval 1286–1338 cm^{-1} reflected a healthy state for the proliferating bacteria. This interpretation was also congruent with the observation that Band 20 (*i.e.*, symmetric stretching of carbonyl groups in amino acid chains) also increased in magnitude.

(iv) Band 27 is related to CH and CH_2 vibrations in peptidoglycans and phospholipids of the membrane structure of the bacteria. This band experienced a dramatic increase in relative intensity with time. Its increase was interpreted as reinforcement of the membrane structure *via* the formation of a biofilm.

In the case of Si_3N_4 (Fig. 5), Zone I was normalized with respect to the polysaccharide Band 1 at ~1030 cm^{-1}. It was the strongest band in this zone and remained conspicuously constant in intensity up to 48 h of exposure. Changes in the spectra during the time-lapse sequence are summarized as follows:

(i) Bands 3–6 (1064–1093 cm^{-1}), which are related to P-containing moieties within the DNA, underwent an initially slight increase at 24 h followed by a successive decrease after 48 h of exposure. In particular, the intensity decrease of Band 4 at 1074 cm^{-1}, which relates to PO_2^- stretching in nucleic acids, suggests degradation of bacteria's DNA structure.[43] Note that, in this spectral region, the differences in Raman intensity between exposed and unexposed bacteria was much less relevant than that recorded for ZTA exposed bacteria (*cf.* dotted line in Fig. 5 overlapped to the 48 h spectrum). The differences between spectra collected from ZTA- and Si_3N_4-exposed bacteria are likely to arise from a different surface chemistry interaction between bacteria and substrates, namely, the different effects of oxygen and nitrogen free radicals on bacterial metabolism. This point will be further discussed in the forthcoming sections 4.1 and 4.2.

(ii) Band 13 at 1225 cm^{-1} (*i.e.*, P═O antisymmetric stretching in PO_2^- phosphodiester) also underwent an initial increase at 24 h followed by a drastic decrease after 48 h exposure. This trend is indicative of bacterial degradation because the gradual disappearance of phosphodiester related bands suggests damage to the bacteria's cell walls.[44] Note that in the 48 spectrum of *S. Epi* exposed to the Si_3N_4 substrate, unlike the case of ZTA substrate tested under the same conditions (*cf.* description of the ZTA spectra given above), we did not detect any preponderance of Bands 10 and 11 related to C–O stretching in carbohydrates. This observation confirms the hypothesis that no appreciable thickening of the outer peptidoglycan layer of the bacterial membrane takes place when bacteria become exposed to the Si_3N_4 substrate.

(iii) The time-lapse trend of Bands 24 and 25, belonging to amino acids, was similar to that of Band 13. They ultimately disappeared after 48 h of exposure.

(iv) Band 27 at ~1455 cm^{-1}, directly related to peptidoglycan, followed the same up and down trend as described in (i)–(iii). This may be interpreted as substantial degradation of the external walls of the bacterial membrane and biofilm at 48 h[44] after an initial proliferation after 24 h exposure to the Si_3N_4 substrate.

(v) The high-frequency Zone II of the time-lapse FTIR spectra of *S. epidermidis* is shown in absolute values in Fig. 6 and 7 for the ZTA and Si_3N_4 substrates, respectively (*cf.* exposure times in the insets to the respective figures). Spectra were recorded under the identical conditions as the control bacteria on glass substrates. For the bacteria exposed to the ZTA substrates, the overall absorbance spectrum kept increasing with time, while it showed an initial increase after 24 h and then a decrease at 48 h for the Si_3N_4-exposed bacteria. This was similar to the trend found in Zone I. The absolute values of absorbance for bacteria on ZTA substrates were even higher than those from the control sample exposed to glass substrate (*cf.* labels in the inset to Fig. 6 and 7 showing the FTIR intensities for the control sample on glass substrate and reported in Fig. 3). This trend for the ZTA substrates was interpreted as confirmation of bacterial proliferation. Regarding the morphology of the spectra in the zone between 1660 and 1780 cm^{-1} (labeled as Bands 40–46), emissions became particularly enhanced with time only for the ZTA-exposed samples. Conversely, the time-lapse behavior for these bands was nearly constant on the glass control samples. An initial intensity increase for Bands 40–46 at 24 h followed by a decrease at 48 h was exhibited by bacteria exposed to Si_3N_4 substrates. Bands 40–42 are Amide I related features (*cf.* Table 2) and their intensity increase and decrease can be ascribed to enhancement and reduction of healthy metabolism in the bacteria, respectively. Conversely, Bands 43–45 are

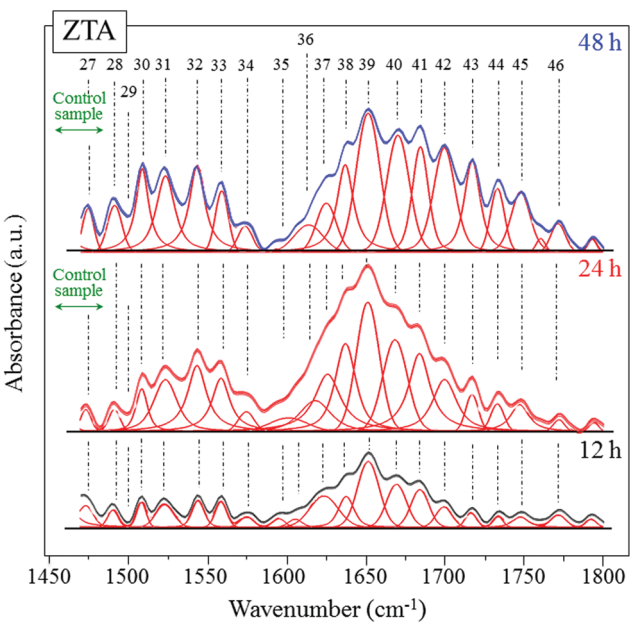

Fig. 6 The FTIR spectral Zone II after normalization on the *S. epidermidis* sample exposed to ZTA substrates for increasing times (*cf.* labels in the inset). The labeling of the sub-bands corresponds to that shown in Table 2.

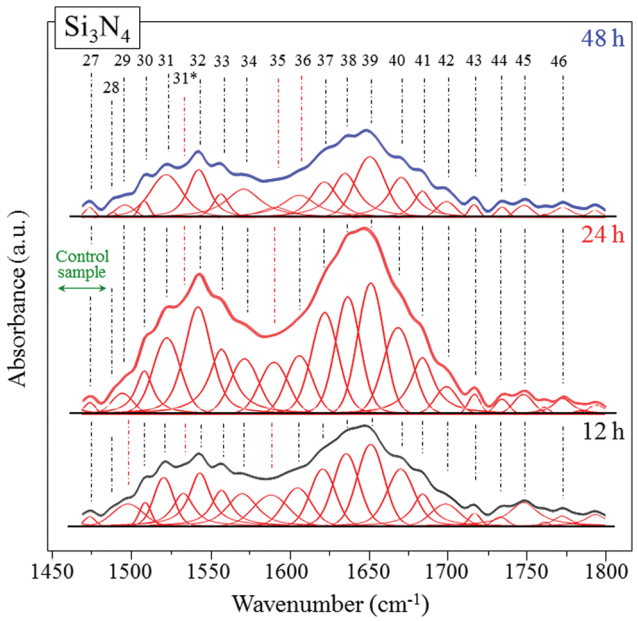

Fig. 7 The FTIR spectral Zone II after normalization on the *S. epidermidis* sample exposed to Si_3N_4 substrates for increasing times (*cf.* labels in the inset). The labeling of the sub-bands corresponds to that shown in Table 2.

mainly due to stretching of carbonic acid bonds in lipids, fatty acids, and esters in the membrane. The strong enhancement of these bands for the ZTA-exposed bacteria can be explained by a thickening of the lipid membrane and an acceleration of biofilm formation. These phenomena were absent in bacteria exposed to control substrates.

For the *S. epidermidis* exposed to the Si_3N_4 substrates, Bands 31–34 (related to Amide II) followed the general trend of the entire FITR spectrum (*cf.* Zone I above) with an initial increase at 24 h followed by a decrease at 48 h. They were also similar to the Amide I Bands 37–42, with the strongest absorbance in Zone II located at ~1630 cm^{-1}. However, the most important feature in Zone II of the spectrum of Si_3N_4-exposed bacteria resided in the appearance of a new band at ~1533 cm^{-1} (labeled as Band 31*), which was clearly resolved only after 12 h of exposure. This new band was due to the presence of COO^- moieties (deprotonated carboxyl groups).[4] Their formation could be related to the consumption of H^+ in order to form ammonia. This process then stops when higher pH values are established in the biological environment surrounding the bacteria. This process was described in section 3.1, in which the reaction of the Si_3N_4 substrate with an acidic environment increased the pH in the surrounding medium.

Deprotonation COO^- in the polysaccharides is denoted by Band 35, located at around 1590 cm^{-1}. Unlike Band 31*, which disappeared at >24 h, Band 35 showed an initial increase at 24 h of exposure before dropping down in intensity after 48 h. It is believed that the difference in time-lapse trend between Bands 31* and 35 is related to a different type of deprotonated moieties in the bacterial cell structure, namely carboxylates *vs.* phosphates.

Note that the trends in FTIR spectra for *S. epidermidis* exposed to Si_3N_4 are in line with the concept that carboxyl, amino, and phosphate groups are the main contributors to the acid–base properties of bacterial cells.[45] It is also conceivable to assume that this pH buffering process and the formation of ammonia associated with Si_3N_4 substrates (*cf.* section 3.1) may have a dramatic impact on the bacteria's metabolism.

4. Discussion

4.1. Protonation/deprotonation reactions peculiar to bioceramic surfaces

In neutral solution (pH~7), Al_2O_3 is chemically stable, and the solubility of its surface generates only minute amounts of hydroxyl aluminum complexes (aluminols; Al–OH, AlO(OH), and $Al(OH)_3$):[46]

$$Al(OH)_3 = Al^{3+}(aq) + 3OH^-(aq)\ (K = 1.9 \times 10^{-33}) \quad (1)$$

where K represents the equilibrium constant of the reaction. However, in an acidic solution, Al_2O_3 and the hydroxyl groups tend to consume protons as follows:[46,47]

$$Al_2O_3 + 6H_3O^+(aq) = 2Al^{3+}(aq) + 9H_2O(l)\ (K = 9.26 \times 10^4) \quad (2)$$

$$AlO(OH) + 3H_3O^+(aq) = Al^{3+}(aq) + 5H_2O(l) \quad (3)$$

$$Al(OH)_3 + 3H_3O^+ = Al^{3+}(aq) + 6H_2O(l)\ (K = 1.9 \times 10^9) \quad (4)$$

Or, represented with the general expression:

$$-Al_n(OH) + H_3O^+(aq) = -Al_n^+ + 2H_2O(l) \quad (5)$$

where n is the coordination of the surface OH species. Accordingly, the pH of the solution slightly increases by the reduction of protons. Conversely, in solutions at pH > 7, Al_2O_3 may slightly decrease the pH by the following reactions:[46]

$$Al_2O_3 + 2OH^-(aq) + H_2O(l) = 2Al(OH)_4^-(aq) \quad (6)$$

$$Al(OH)_3 + OH^-(aq) = Al(OH)_4^-(aq) \quad (7)$$

$$AlO(OH) + OH^-(aq) + H_2O(l) = Al(OH)_4^-(aq) \quad (8)$$

In substance, in an initial neutral solution of the bacterial/substrate, reactions at the surface of Al_2O_3 help balance pH; but they have a reduced role when bacteria significantly proliferate and acidic pH shifts become preponderant. As could be seen from eqn (2)–(8), even under a severe environmental acidification, the effect of proton consuming tends to undergo counterbalancing as soon as the pH reaches a neutral value. Moreover, the eventual formation of biofilm might limit the ionic exchange at the substrate–solution interface, as the antimicrobial action can only be fully exploited upon direct contact between surface and bacteria. This is the reason why no substantial pH-buffering effect around the Al_2O_3 substrate was observed when it was exposed to the acidic environment (*cf.* Fig. 2).

In the case of Si_3N_4, exposure to an aqueous solution results in the following surface reactions:[48]

$$Si_3N_4 + 6H_2O(l) = 3SiO_2 + 4NH_3(aq) \quad (9)$$

$$SiO_2(s) + 2H_2O(l) = Si(OH)_4 \quad (10)$$

The overall reaction is strongly pH dependent and could be expressed as:

$$Si_3N_4 + 12H_2O(l) = 3Si(OH)_4 + 4NH_3(aq) \quad (11)$$

The Gibbs energy ΔG_f^{298} of the above reaction (11) has been reported to be −1268.72 kJ mol^{-1} (ref. 48) and to relate to the equilibrium constant, K, according to the following equation:

$$\Delta G = -2.303RT \times \log K \quad (12)$$

where R is the gas constant and T is the temperature. The equilibrium constant of the above equation at room temperature thus becomes: $K = 1.57 \times 10^{96}$.

A comparison with the pH-buffering capacity of Al_2O_3 ($K = 1.9 \times 10^9$; *cf.* reaction (4) above) shows that reactions at the Si_3N_4 substrate surface predominant and are faster than those at the surface of Al_2O_3 substrates. Thus, non-oxide Si_3N_4 is better able to counteract the acidic environment associated with bacterial proliferation. The non-oxide lattice is less stable than the oxide due to the homolytic cleavage of the covalent bond between Si and N. However, this instability happens to be a desirable event for biomedical applications. This pH-buffering effect is directly related to the formation of ammonia. Note that in an acidic environment, dissolution of amphoteric silica takes place through migration of silanol adsorbates, Si–OH, from the surface to form silicic acid, $Si(OH)_4$ (*cf.* eqn (10)). Because it is unstable in water, $Si(OH)_4$ condenses into polymeric chains. With progressive dissolution of amphoteric silica, the statistical population of amine adsorbates (Si_2–NH and Si–NH) on the Si_3N_4 surface increases and attracts protons to form ammonia, NH_3. A strong driving force to produce ammonia induces an influx of protons toward the adsorbed amine species, which depletes the solution of protons and raises the local pH at the solid/liquid interface. Per reaction (13), a portion of the released ammonia reacts with water to form NH_4^+ and OH^-,[49] further increasing local pH.

$$NH_3(aq) + H_2O(l) = NH_4^+(aq) + OH^-(aq) \ (K = 1.8 \times 10^{-5}) \quad (13)$$

The non-linear nature of the pH plot displayed in Fig. 2 for the Si_3N_4 substrates could be interpreted according to this sequence of chemical events. According to kinetics considerations based on ref. 46 and 47, the initial rise and saturation of the plot at $t < 20$ min reflects dissolution of the initial layer of amphoteric silica to form silicic acid, while the successive rise and saturation pattern at $t > 20$ min represents the migration of protons toward the amine adsorbates on the Si_3N_4 surface. Note also that the rate at which the pH rises around the Si_3N_4 sample decreases with decreasing initial acidity of the medium, since both the speed at which amphoteric silica dissolves and the concentration of protons are inversely related to local pH. The initial environment to which bacteria are exposed on the testing substrates is less acidic than the *in situ* pH microscopy experiments. Bacterial proliferation's tendency to induce local acidification is counteracted by the substrate pH buffering effect. However, in order to activate this buffering, an initial drift of the environment toward acidic pH *via* commencement of bacterial proliferation is needed. This is indeed what was observed in the current *in vitro* experiments. They showed an initial increase in bacterial activity at 24 h of exposure followed by their reduction and lysis at 48 h. Accordingly, we believe that the time threshold after which bacterial lysis starts is dictated by the kinetics of ammonia elution from the Si_3N_4 surface, which in turn is pH dependent (*i.e.*, the concentration of eluted ammonia increases with decreasing environmental pH). From this viewpoint, Si_3N_4 could be considered an "intelligent" substrate since it elutes more bactericidal ammonia as the bacterial population increases (*i.e.*, the pH in its surroundings decreases) and *vice versa*.

4.2. Spectroscopic fingerprints for the effects of substrates on bacteria

Carboxyl groups. FTIR is selective for carboxyl groups in organic macromolecules.[2] The large polarity of the C–O bond, which results in its high infrared activity, produces strong and pH-dependent vibrational bands. Dissimilarity in the C–O bonds of a protonated carboxyl group is the origin of independent vibrational modes for C═O and C–OH. The stretching mode of the former bonds is at ~1690 and 1750 cm^{-1}, while the latter bonds present a mix of stretching and bending modes between 1200 and 1450 cm^{-1}. The overlap produces a broad absorption peak which is difficult to identify; this situation is further complicated by the presence of H-bonding with molecules from the environment.[50] However, deprotonation of carboxylic acid alters the bond balance forcing the electron density to be equally shared between the two equivalent C–O bonds of the carboxylate anion. Accordingly, symmetric and antisymmetric stretching modes of C–O in the carboxylate moiety become distinct features in the FTIR spectrum at frequency intervals 1300–1420 and 1540–1650 cm^{-1}, respectively.[50–52] The antisymmetric stretching absorbance has long been considered as the most suitable probe of carboxylation because it is less susceptible to vibrational coupling.[53,58] Fig. 8(a) shows a schematic model of the vibrational behavior of carboxylic acid and the carboxylate anion. Hay and Myneni[54] compiled a useful list of carboxylate anion vibrational energies for a variety of aliphatic and aromatic carboxylates. Their compilation demonstrates the correlation between antisymmetric stretching vibrations and chemical structure of carboxylated ions. More specifically, a linear correlation was found between the C–O antisymmetric stretching frequency in carboxylated ions and environmental pH in the bacterial surroundings.

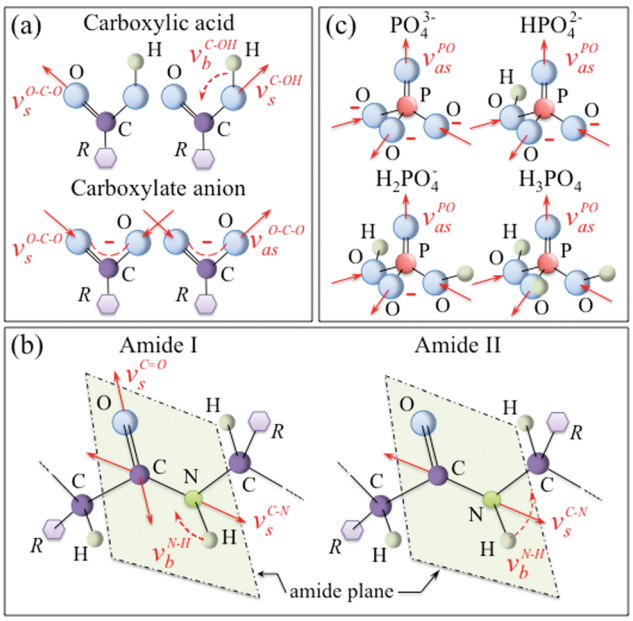

Fig. 8 Schematic models of: (a) vibrational behavior of carboxylic acid and carboxylate anion; (b) vibrational modes in the Amide I and Amide II regions; and, (c) vibrational behavior of protonated and deprotonated phosphate groups. Vibrations are generically indicated as ν, with the subscript indicating the type of vibration (s, as, and b for symmetric stretching, antisymmetric stretching, and bending, respectively) and the superscript locating the vibrating bond.

These basic notions can now be used to interpret the vibrational spectroscopy data associated within the current FTIR experiments. The primary building blocks in the walls of Gram-positive bacterial cells are the peptidoglycans (*e.g.*, polymeric chains of *N*-acetylglucosamine and *N*-acetylmuramic acid). These chains contain carboxyl, amide, and hydroxyl functional groups in addition to teichoic acid (a polymer of glycopyranosyl glycerol phosphate) and teichuronic acid. This latter compound is similar to teichoic acid, but contains phosphate functional groups to replace carboxyls.[35] Several major proton-active functional groups are contained in the above constituents of the bacteria's cell surface. Within acidic solutions, the carboxylic acid groups, C═O and C–OH bonds of the –COOH group exhibit vibrational bands at 1728 and 1268 cm^{-1}, respectively. However, upon increasing pH, these bands decrease in intensity, while two new bands appear at 1589 and 1413 cm^{-1}, corresponding to antisymmetric and symmetric stretching vibrations of deprotonated COO^- groups, respectively.[37] In the current experiments, C═O and C–OH vibrations in the –COOH group were labeled as Bands 44 (seen at 1735 cm^{-1}) and 16 (seen at 1268 cm^{-1}), respectively. The absorbance due to deprotonated COO^- groups corresponded to Bands 35 (seen at 1590 cm^{-1}) and 25 (seen at 1417 cm^{-1}), respectively. When bacteria proliferated on ZTA substrates, the relative intensities of Bands 44 and 16 monotonically increased with elapsing exposure time (*cf.* Fig. 6 and 4). This was interpreted the progressive establishment of an acidic environment together with bacteria proliferation. Conversely, in bacteria experiments on Si_3N_4 substrates, carboxylate vibrations were not preponderant (*cf.* Fig. 7 and 5) during the entire experiment because of the pH buffering effect discussed in section 4.1. As expected, bacteria cultured on ZTA substrates in the acidic environment showed low intensity for Band 35 at 1590 cm^{-1} over the entire time-span of the test. Yet, there was increasing (relative) absorbance with time for Band 25 at 1417 cm^{-1}. This feature, which was not expected in acidic environment,[37] was ascribed to frequency overlap with in-plane bending of C–OH units which were also affected by molecules from the environment.[50]

Amide groups. The amide groups exhibited intense absorptions at ~1650 and 1550 cm^{-1} corresponding to the Amide I and Amide II vibrations, respectively (Fig. 8(b)). Both energies and intensities of these bands are reported in literature to be negligibly affected by pH changes.[2] However, the intensity ratio of Amide I to Amide II decreases with increasing pH as a minor variation.[2] This change was ascribed to the possible appearance of new peaks related to COO^- groups in this energy region. In the current experiments, the absorbance of Amide I and II appeared at 1652 and 1545 cm^{-1}, and were labeled as Bands 39 and 32, respectively. The ratio of the absorbance of Amide I to Amide II (intensity of Band 39 over Band 32) remained constant at a ratio ~2 up to 24 h, but a clear increase to ~2.3 was detected after 48 h for bacteria exposed to the ZTA substrates. This feature suggested a decrease in pH of the environment due to bacteria proliferation. However, for bacteria exposed to Si_3N_4, the intensity ratio of Band 39 to Band 32 clearly decreased with exposure time from 12 to 24 h (from ~1.55 to ~1.2) and then remained constant up to 48 h. This spectroscopic feature was due to pH buffering by Si_3N_4 and was corroborated through independent experiments in section 3.1 and discussed in section 4.1. This effect was due to the appearance of a new band at ~1530 cm^{-1}, labeled as Band 31* (*cf.* Fig. 7). It was attributed to antisymmetric vibrations of deprotonated carboxyl groups COO^-.[39]

Phosphate groups. Phosphate groups are important constituents of bacterial cells. They coexist in inorganic (orthophosphate and its oligomers) and organic (phosphate monoesters and diesters) forms. Earlier investigations for basic compounds in aqueous environments[30,31] located antisymmetric stretching vibrations of PO_4^{3-} at around 1010 cm^{-1} as a function of pH. Upon protonation, the antisymmetric stretching vibration frequencies shifted to 1077, 1155, and 1174 cm^{-1} in the case of HPO_4^{2-}, $H_2PO_4^-$, and neutral H_3PO_4, respectively (Fig. 8(c)). Regarding phosphate oligomers, which include pyrophosphate, $O_3P–O–PO_3^{4-}$, and tripolyphosphate, $O_3P–O–PO_3–PO_3^{5-}$, the antisymmetric stretching modes of the deprotonated groups can be found in the range 1160–1240 cm^{-1}. Upon deprotonation, the absorbance band of protonated tripolyphosphate at around 1240 cm^{-1} decreases in intensity and shifts to lower energies by about 40 cm^{-1} as a consequence of the weakening of the P═O bond. The bands related to P–OH and P–O–P from protonated phosphates appear at 850–1010 cm^{-1}. Although in principle they are sensitive to deprotonation, they have been reported to have strongly overlapping absorbance from carbohydrates,[2] thus ren-

dering the quantification of these moieties' deprotonation by vibrational analyses difficult.

Translating these basic notions into the output of the present spectroscopic experiments, it was noticed that PO_4^{3-} vibrations were weak (low absorbance activity at ~1010 cm^{-1}), if not absent, for both ZTA- and Si_3N_4-exposed samples. However, a dramatic increase in Bands 10 and 11 (1165 and 1182 cm^{-1}, respectively) were observed only for bacteria exposed to ZTA after 48 h. The absorbance frequencies of these bands lie close to those of $H_2PO_4^-$ and neutral H_3PO_4 in protonated phosphate groups, respectively. Moreover, a new band (labeled as Band 4^- in Fig. 4) appeared at ~1072 cm^{-1} after 48 h exposure. Its energy corresponded to vibrations of HPO_4^{2-}. These spectral features are due to chemical species that only exist in a substantially acidic environment. It is assumed that they are evidence for the acidic pH developed by proliferating *S. epidermidis* on the surface of the ZTA substrate. Conversely, for bacteria exposed to Si_3N_4 substrates, the quite low intensity of Band 11 regardless of exposure suggests establishment of an alkaline environment. Band 14 (at ~1240 cm^{-1}), which is representative of protonated polyphosphates, exhibited low intensity for both ZTA and Si_3N_4. This effect is conceivable if one considers that the membrane of Gram-positive bacteria primarily consists of peptidoglycans. However, it should be noted that observations of the deprotonation process at around 1200 cm^{-1} was challenging for both substrate materials due to the overall low absorbance intensity and a frequency overlap with ring vibrations from different moieties (*e.g.*, the C–OH bonds of carboxylic acids) which absorb in the same energy region. Nevertheless, the high relative intensity of the C–O stretching Band 11 after 48 h exposure to the ZTA substrate as compared to that of the same band after 48 h exposure to the Si_3N_4 substrate is interpreted here as a clear sign of the different impact of the eluted oxygen and nitrogen free radicals on *S. epidermidis* metabolism (*cf.* Fig. 4 and 5). The oxygen radicals eluted from the ZTA substrate (*cf.* above eqn (2)–(8)) mainly impact on the external peptidoglycan wall of the bacterial membrane. The bacteria then react to this surface attack by thickening their external wall. They eventually succeed in proliferating and forming a protective biofilm enclave. On the other hand, *S. epidermidis* bacteria initially do not feel any significant attack from the chemical species eluted from the Si_3N_4 substrate (*cf.* above eqn (9)–(11)) and, consequently, show no thickened walls in response to it. However, after experiencing an apparently friendly environment in the initial period of exposure, ammonia elution eventually rises up as their proliferation lowers environmental pH. Upon directly penetrating the bacterial membrane, NH_3 ultimately poisons the bacteria, incapable to metabolize NO free-radical byproducts (produced in the intracellular space upon monooxygenase/oxidoreductase,[55,56] as discussed in detail in the companion paper[23]).

4.3. The importance of non-oxide ceramics in prosthetic implants

The inert nature of bioceramics has been advertised as a major safety advantage in prosthetic implants.[57] However, contrary to this general concept, the data presented herein demonstrated that the bioinertness paradigm does not apply to non-oxide Si_3N_4 bioceramics; their inherent non-bioinertness can be exploited to mitigate prosthetic infections.

The stability of ionic Al–O bonds and the low reactivity of aluminols in an aqueous environment are in stark contrast with the cleavage tendency of covalent Si–N bonds and the migration of silanol adsorbates. These represent fundamental differences between oxide and non-oxide bioceramics. The spectroscopic results of this study suggest that the long-term antibacterial response of non-oxide ceramics may be more beneficial than the simple passive bony apposition observed on oxide surfaces. Previously published studies[58–61] have also elucidated the fundamental role orthosilicic acid plays in facilitating a range of favorable metabolic interactions between both eukaryotic and prokaryotic cells. This compound promoted osteoblast differentiation and osteogenesis at the silicon nitride surface. Si_3N_4 ceramics have demonstrated enhanced osteointegration in animal studies[62,63] and in a case report study of a human cervical spinal implant after 11 months *in vivo*.[64] Finally, it should be emphasized that finding a synthetic biomaterial whose surface chemistry concurrently enhances antibacterial and osteogenic behaviors is a rare find. From this viewpoint, Si_3N_4 may be a unique example among biomaterials; it's use might signal a shift from "passive bionic" toward "active healing" prosthetic implants. The discovery of its friendly surface chemistry calls for updated scientific criteria that trigger advanced research into new potential "medicinal" materials.

5. Conclusion

The metabolism of *S. epidermidis* exposed to oxide ZTA and non-oxide Si_3N_4 ceramics has been analyzed in time-lapse experiments by *in situ* FTIR spectroscopy. This study corroborated the conclusions presented in a companion paper in which *S. epidermidis* was exposed to ceramic substrates and studied by Raman spectroscopy. FTIR spectral changes were compared with those reported in literature for model molecules of carboxylic, amide, and phosphate groups. These moieties exhibited dominant changes at around 1720, 1500–1700, and 1200 cm^{-1}, respectively. C–C skeletal vibrations in carbohydrates did not exhibit significant changes upon exposure time and type of substrate. However, variations of amide, common in the protein backbone, and phosphate groups strongly depended on time and type of substrate. Vibrations of molecules containing amides, which included the C═O bending of Amide I and the N–H bending (coupled to C–N) of Amide II, clearly reflected inverse trends for bacteria exposed to ZTA and Si_3N_4 substrates by suggesting pH shifts in the bacterial environment toward acidic and alkaline values, respectively. The acidic pH trend upon exposure to the ZTA substrate was also confirmed by features in the vibrational behavior of carboxylic acid groups and phosphates, as follows: (i) as expected, C═O and C–OH bonds of the –COOH group

increased in intensity with increasing exposure time in the acidic environment created by *S. epidermidis* proliferation; and, (ii) there was an observed increase in the absorbance activity from protonated phosphate groups; these moieties only exist in acidic environments. None of the above spectroscopic patterns were observed upon exposure of bacteria to Si_3N_4 substrates under the same experimental conditions. Direct pH microscopy observations of ceramic substrates exposed to an acidic environment confirmed the occurrence of a pH buffering effect with Si_3N_4 but not Al_2O_3.

In conclusion, this study has explored features of the FTIR spectra associated with time-lapse changes in bacterial moieties as they reacted with the surfaces of oxide and non-oxide ceramic substrates. It was demonstrated that non-oxide ceramics are capable of peculiar chemical reactions that inhibit the spread of common periprosthetic infections.

Conflicts of interest

Giuseppe Pezzotti is a consultant to Amedica Corporation, Bryan J. McEntire and B. Sonny Bal work at Amedica Corporation.

References

1 U. Neugebauer, U. Schmid, K. Baumann, W. Ziebuhr, S. Kozitskaya, V. Deckert, *et al.*, Towards a Detailed Understanding of Bacterial Metabolism—Spectroscopic Characterization of *Staphylococcus epidermidis*, *ChemPhysChem*, 2007, **8**, 124–137.

2 W. Jiang, A. Saxena, B. Song, B. B. Ward, T. J. Beveridge and S. C. Myneni, Elucidation of functional groups on gram-positive and gram-negative bacterial surfaces using infrared spectroscopy, *Langmuir*, 2004, **20**, 11433–11442.

3 D. Helm, H. Labischinski, G. Schallehn and D. Naumann, Classification and identification of bacteria by Fourier-transform infrared spectroscopy, *J. Gen. Microbiol.*, 1991, **137**, 69–79.

4 B. Buszewski, E. Dziubakiewicz, P. Pomastowski, K. Hrynkiewicz, J. Ploszaj-Pyrek, E. Talik, M. Kramer and K. Albert, Assignment of functional groups in Gram-positive bacteria, *J. Anal. Bioanal. Tech.*, 2015, **6**, 232.

5 E. Aboualizadeh, V. V. Bumah, D. S. Masson-Meyers, J. T. Eells, C. J. Hirschmugl and C. S. Enwemeka, Understanding the antimicrobial activity of selected disinfectants against methicillin-resistant *Staphylococcus aureus* (MRSA), *PLoS One*, 2017, **12**, e0186375.

6 D. Morita, H. Sawada, W. Ogawa, H. Miyachi and T. Kuroda, Riccardin C derivatives cause cell leakage in *Staphylococcus aureus*, *Biochim. Biophys. Acta*, 2015, **1848**, 2057–2064.

7 M. C. Sportelli, E. Tutuncu, R. A. Picca, M. Valentini, A. Valentini, C. Kranz, B. Mizaikoff, H. Barth and N. Cioffi, Inhibiting *P. fluorescens* biofilms with fluoropolymer-embedded silver nanoparticles: an *in-situ* spectroscopic study, *Sci. Rep.*, 2017, **7**, 11870.

8 E. J. Elzinga, J.-H. Huang, J. Chorover and R. Kretzschmar, ATR-FTIR spectroscopy study of the influence of pH and contact time on the adhesion of *Shewanella putrefaciens* bacterial cells to the surface of hematite, *Environ. Sci. Technol.*, 2012, **46**, 12848–12855.

9 U. Neugebauer, U. Schmid, K. Baumann, W. Ziebuhr, S. Kozitskaya, U. Holzgrabe, M. Schmitt and J. Popp, The influence of fluoroquinolone drugs on the bacterial growth of *S. epidermidis* utilizing the unique potential of vibrational spectroscopy, *J. Phys. Chem. A*, 2007, **111**, 2898–2906.

10 L. Mikoliunaite, R. D. Rodriguez, E. Sheremet, V. Kolchuzhin, J. Meher, A. Ramanavicius and D. R. T. Zahn, The substrate matters in the Raman spectroscopy analysis of cells, *Sci. Rep.*, 2015, **5**, 13150.

11 B. Stuart, *Infrared Spectroscopy: Fundamentals and Applications*, John Wiley & Sons, Ltd., Chichester, UK, 2004, pp. 137–163.

12 J. F. M. Almarashi, N. Kapel, T. S. Wilkinson and H. H. Telle, Raman spectroscopy of bacterial species and strains cultivated under reproducible conditions, *Spectrosc. Int. J.*, 2012, **27**, 361–365.

13 O. Samek, J. F. M. Al-Marashi and H. H. Telle, The potential of Raman spectroscopy for the identification of biofilm formation by *Staphylococcus epidermidis*, *Laser Phys. Lett.*, 2010, **7**, 378–383.

14 G. Pezzotti, R. M. Bock, B. J. McEntire, E. Jones, M. Boffelli, W. Zhu, G. Baggio, F. Boschetto, L. Puppulin, T. Adachi, T. Yamamoto, N. Kanamura, Y. Marunaka and B. S. Bal, Silicon nitride bioceramics induce chemically driven lysis in *Porphyromonas Gingivalis*, *Langmuir*, 2016, **32**, 3024–3035.

15 U. C. Schröder, A. Ramoji, U. Glaser, S. Sachse, C. Leiterer, A. Csaki, U. Hübner, W. Fritzsche, W. Pfister, M. Bauer, J. Popp and U. Neugebauer, Combined dielectrophoresis – Raman setup for the classification of pathogens recovered from the urinary tract, *Anal. Chem. II*, 2013, **85**, 10717–10724.

16 E. E. MacKintosh, J. D. Patel, R. E. Marchant and J. M. Anderson, Effects of biomaterial surface chemistry on the adhesion and biofilm formation of *Staphylococcus epidermidis in vitro*, *J. Biomed. Mater. Res., Part A*, 2006, **78**, 836–842.

17 C. R. Arciola, D. Campoccia and L. Montanaro, Detection of biofilm-forming strains of *Staphylococcus epidermidis* and *S. aureus*, *Expert Rev. Mol. Diagn.*, 2002, **2**, 478–484.

18 J. W. Costerton, K. J. Cheng, G. G. Geesey, T. I. Ladd, J. C. Nickel, M. Dasgupta and T. J. Marrie, Bacterial biofilms in nature and disease, *Annu. Rev. Microbiol.*, 1987, **41**, 435–464.

19 L. Pulido, E. Ghanem, A. Joshi, J. J. Purtill and J. Parvizi, Periprosthetic joint infection: the incidence, timing, and predisposing factors, *Clin. Orthop. Relat. Res.*, 2008, **466**(7), 1710–1715.

20 T. J. Foster and D. McDevitt, Molecular basis of adherence of staphylococci to biomaterials, in *Infection associated with indwelling medical devices*, ed. A. L. Bisno and F. A. Waldvogel, American Society for Microbiology, Washington, DC, USA, 2nd edn, 1994, pp. 31–43.
21 Y. H. An and R. J. Friedmann, Concise review of mechanisms of bacterial adhesion to biomaterial surfaces, *J. Biomed. Mater. Res.*, 1998, **43**, 338–348.
22 L. Montanaro and C. R. Arciola, Studying bacterial adhesion to irregular or porous surfaces, in *Handbook of bacterial adhesion: principles, methods and applications*, ed. Y. H. An and R. J. Friedmann, Humana Press Inc., Totowa, NJ, USA, 2000, pp. 331–343.
23 G. Pezzotti, R. M. Bock, B. J. McEntire, T. Adachi, E. Marin, F. Boschetto, W. Zhu, O. Mazda and B. S. Bal, In vitro antibacterial activity of oxide and non-oxide bioceramics for arthroplastic devices: I. In situ time-lapse Raman spectroscopy, *Analyst*, submitted.
24 R. M. Bock, B. J. McEntire, B. S. Bal, M. N. Rahaman, M. Boffelli and G. Pezzotti, Surface modulation of silicon nitride ceramics for orthopaedic applications, *Acta Biomater.*, 2015, **26**, 318–330.
25 W. Burger and H. G. Richter, High strength and toughness alumina matrix composites by transformation toughening and 'in situ' platelet reinforcement (ZPTA) - The new generation of bioceramics, in *Proceedings of the 13th International Symposium on Ceramics in Medicine*, ed. S. Giannini and A. Moroni, Trans Tech Publications, Zürich, 2000, pp. 545–548.
26 Y. Kitasako, T. Nikaido, J. Tagami, K. Ikeda, K. Mitsunari and S. Nomura, Surface analysis of human teeth using a pH imaging microscope based on a semiconductor silicon sensor, *Bunseki Kagaku*, 2000, **49**, 325–327.
27 A. Bosch, D. Serra, C. Prieto, J. Schmitt, D. Naumann and O. Yantorno, Characterization of *Bordatella pertussis* growing as biofilm by chemical analysis and FT-IR spectroscopy, *Appl. Microbiol. Biotechnol.*, 2005, **16**, 1–12.
28 A. Karadenizli, F. Kolayli and K. Ergen, A novel application of Fourier-transformed infrared spectroscopy: classification of slime from Staphylococci, *Biofouling*, 2007, **23**, 63–71.
29 G. L. Huang, Extraction of two active polysaccharides from the yeast cell wall, *Z. Naturforsch., C: Biosci.*, 2008, **63**, 919–921.
30 P. Persson, N. Nilsson and S. Sjoberg, Structure and bonding of orthophosphate ions at the iron oxide–aqueous interface, *J. Colloid Interface Sci.*, 1996, **177**, 263–275.
31 K. Nakamoto, *Infrared and Raman Spectra of Inorganic and Coordination Compounds*, Wiley, New York, 1986.
32 K. Maquelin, C. Kirschner, L.-P. Choo-Smith, N. van den Braak, H. Ph. Endtz, D. Naumann and G. J. Puppels, Identification of medically relevant microorganisms by vibrational spectroscopy, *J. Microbiol. Methods*, 2002, **51**, 255–271.
33 K. Krishnamurthy, J. C. Tewari, J. Irudayaraj and A. Demirci, Microscopic and spectroscopic evaluation of inactivation of *Staphylococcus aureus* by pulsed UV light and infrared heating, *Food Bioprocess Technol.*, 2010, **3**, 93–104.
34 F. Faghihzadeh, N. M. Anaya, L. A. Schifman and V. Oyanedel-Craver, Fourier transform infrared spectroscopy to assess molecular-level changes in microorganisms exposed to nanoparticles, *Nanotechnol. Environ. Eng.*, 2016, **1**, 1–16.
35 T. J. Berveridge, Ultrastructure, chemistry, and function of the bacterial wall, *Int. Rev. Cytol.*, 1981, **72**, 229–317.
36 J. P. Maity, S. Kar, C.-M. Lin, C.-Y. Chen, Y.-F. Chang, J.-S. Jean and T. R. Kulp, Identification and discrimination of bacteria using Fourier transform infrared spectroscopy, *Spectrochim. Acta, Part A*, 2013, **116**, 478–484.
37 T. J. Strathmann and S. C. B. Myneni, Speciation of aqueous Ni(II)-carboxylate and Ni(II)-fulvic acid solutions: Combined ATR-FTIR and XAFS analysis, *Geochim. Cosmochim. Acta*, 2004, **68**, 3441–3458.
38 M. Silverstein, G. Clayton Basseler and C. Morrill, *Spectrometric identification of organic Compounds*, John Wiley, New York, USA, 1991.
39 C. Koutsoupakis, T. Soulimane and C. Varotsis, Probing the Q-proton pathway of ba_3-cytochrome *c* oxidase by time-resolved Fourier transform infrared spectroscopy, *Biophys. J.*, 2004, **86**, 2438–2444.
40 L. Marcotte, G. Kagalaer, C. Sandt, J. Barbeau and M. Lafleur, An alternative infrared spectroscopy assay for the quantification of polysaccharides in bacteria samples, *Anal. Biochem.*, 2007, **361**, 7–14.
41 P. Hellwig, B. Rost, U. Kaiser, C. Ostermeier, H. Michel and M. Werner, Carboxyl group protonation upon reduction of the *Paracoccus denitrificans* cytochrome *c* oxidase: direct evidence by FTIR spectroscopy, *FEBS Lett.*, 1996, **385**, 53–57.
42 F. Quiles, S. Saadi, G. Francius, J. Bacharouche and F. Humbert, *In situ* and real time investigation of a *Pseudomonal fluorescens* nascent biofilm in the presence of an antimicrobial peptide, *Biochim. Biophys. Acta*, 2016, **1858**, 75–84.
43 A. Pevsner and M. Diem, Infrared spectroscopic studies of Major cellular components. Part II: The effect of hydration on the spectra of nucleic acids, *Appl. Spectrosc.*, 2001, **55**, 1502–1505.
44 X. Lu, B. A. Rasco, J. M. F. Jabal, D. E. Aston, M. Lin and M. E. Konkel, Investigating antibacterial effects of garlic (*Allium sativum*) concentrate and garlic-derived organosulfur compounds on *Campylobacter jejuni* by using Fourier transform infrared spectroscopy, Raman spectroscopy, and electron microscopy, *Appl. Environ. Microbiol.*, 2011, **77**, 5257–5269.
45 E. Dziubakiewicz, K. Hrynkiewicz, M. Walczyk and B. Buszewski, Study of charge distribution on the surface of biocolloids, *Colloids Surf., B*, 2013, **104**, 122–127.
46 C. K. Gupta, *Chemical Metallurgy: Principles and Practice*, Wiley-VCH, 2004, DOI: 10.1002/3527602003.
47 E. McCafferty, *Introduction to Corrosion Science*, Springer, 2010, DOI: 1007/978-1-4419-0454-6.
48 F. Zhou, X. Wang, K. Adachi and K. Kato, Influence of normal load and sliding speed on the tribological property of amorphous carbon nitride coatings sliding against Si_3N_4 balls in water, *Surf. Coat. Technol.*, 2008, **202**, 3519–3528.

49 R. Petrucci and W. Harwood, *General Chemistry: Principles & Modern Applications*, Macmillan Publishing Company, New York, New York, USA, 6th edn, 1993.
50 S. E. Cabaniss, J. A. Leenheer and I. F. McVey, Aqueous infrared carboxylate absorbances: aliphatic di-acids, *Spectrochim. Acta, Part A*, 1998, **54**, 449–458.
51 P. R. Pike, P. A. Sworan and S. E. Cabaniss, Quantitative aqueous attenuated total reflectance Fourier transform infrared spectroscopy. Part II. Integrated molar absorptivities of alkyl carboxylates, *Anal. Chim. Acta*, 1993, **280**, 253–261.
52 S. E. Cabaniss and I. F. McVey, Aqueous infrared carboxylate absorbances: aliphatic monocarboxylates, *Spectrochim. Acta, Part A*, 1995, **51**, 2385–2395.
53 E. C. Yost, M. I. Tejedor-Tejedor and M. A. Anderson, *In situ* CIR-FTIR characterization of salicylate complexes at the goethite/aqueous solution interface, *Environ. Sci. Technol.*, 1990, **24**, 822–828.
54 M. B. Hay and S. C. B. Myneni, Structural environments of carboxyl groups in natural organic molecules from terrestrial systems. Part 1: Infrared spectroscopy, *Geochim. Cosmochim. Acta*, 2007, **71**(14), 3518–3532.
55 D. J. Arp and L. Y. Stein, Metabolism of inorganic N compounds by ammonia-oxidizing bacteria, *Crit. Rev. Biochem. Mol. Biol.*, 2003, **38**, 471–495.
56 L. Y. Stein and Y. L. Yung, Production, isotopic composition, and atmospheric fate of biologically produced nitrous oxide, *Annu. Rev. Earth Planet. Sci.*, 2003, **31**, 329–356.
57 Ceramtec. BIOLOX®delta Scientific Information and Performance Data, available at: http://pdf.directindustry.com/pdf/ceramtec/bioloxdelta-fourth-generation-ceramics/5715-575903.html (accessed on April 7, 2018).
58 G. Pezzotti, B. J. McEntire, R. Bock, M. Boffelli, W. Zhu, E. Vitale, L. Puppulin, T. Adachi, T. Yamamoto, N. Kanamura and B. S. Bal, Silicon nitride: a synthetic mineral for vertebrate biology, *Sci. Rep.*, 2016, **6**, 31717.
59 G. Pezzotti, E. Marin, T. Adachi, A. Rondinella, F. Boschetto, W. Zhu, N. Sugano, R. M. Bock, B. McEntire and B. S. Bal, Bioactive silicon nitride: a new therapeutic material for osteoarthropathy, *Sci. Rep.*, 2017, **7**, 44848.
60 G. Pezzotti, B. J. McEntire, R. Bock, W. Zhu, F. Boschetto, A. Rondinella, E. Marin, Y. Marunaka, T. Adachi, T. Yamamoto, N. Kanamura and B. S. Bal, In situ spectroscopic screening of osteosarcoma living cells on stoichiometry-modulated silicon nitride bioceramic surfaces, *ACS Biomater. Sci. Eng.*, 2016, **2**, 1121–1134.
61 G. Pezzotti, R. M. Bock, T. Adachi, A. Rondinella, F. Boschetto, W. Zhu, E. Marin, B. McEntire, B. S. Bal and O. Mazda, Silicon nitride surface chemistry: a potent regulator of mesenchymal progenitor cell activity in bone formation, *Appl. Mater. Today*, 2017, **9**, 82–95.
62 T. J. Webster, A. A. Patel, M. Rahaman and B. S. Bal, Anti-infective and osteointegration properties of silicon nitride, poly (ether ether ketone), and titanium implants, *Acta Biomater.*, 2012, **8**, 4447–4454.
63 M. Anderson and R. Olsen, Bone ingrowth into porous silicon nitride, *J. Biomed. Mater. Res., Part A*, 2010, **92**, 1598–1605.
64 G. Pezzotti, N. Oba, W. Zhu, E. Marin, A. Rondinella, F. Boschetto, B. McEntire, K. Yamamoto and B. S. Bal, Human osteoblasts grow transitional Si/N apatite in quickly osteointegrated Si_3N_4 cervical insert, *Acta Biomater.*, 2017, **64**, 411–420.